

# Amorphous Boron Nitride Nanosheet-Based Solid State Electrolytes with High Ionic Conductivity

Yue Fang,<sup>[a]</sup> Yeba Yan,<sup>[a]</sup> Xinying Wang,<sup>[a]</sup> Zhihong Zhang,<sup>[c]</sup> Libin Tian,<sup>[d]</sup> Shengguo Lu,<sup>[a]</sup> Bo Liang,<sup>[a]</sup> Yingbang Yao,<sup>[a]</sup> Daniel Q. Tan,<sup>[b]</sup> Shaoming Huang,<sup>[a]</sup> and Tao Tao<sup>\*[a, c]</sup>

Amorphous boron nitride nanosheets, with natural electrical insulation, outstanding chemical stability and mechanical properties, are introduced as a matrix to be incorporated with lithium bis (trifluoromethanesulfonyl) imide (LiTFSI) and polymer polyvinylidene fluoride-hexafluoropropylene copolymer (PVDF-HFP), for constructing a novel composite solid-state electrolyte by a simple solution-casting method. Amorphous boron nitride nanosheets are produced via a combination method of ball milling and pure water exfoliation. The obtained composite solid-state electrolyte containing 40% (mass fraction) PVDF-HFP shows a high lithium ion conductivity ( $1.936 \times 10^{-3} \text{ S cm}^{-1}$ ) and lithium ion transference number (0.47), and a wide electrochemical stability window (5 V) at room

temperature. The LiFePO<sub>4</sub>/Li based all solid-state battery, consisting of the composite solid electrolyte (40% PVDF-HFP), delivers a capacity of 128.1 mAh g<sup>-1</sup>, a Coulombic efficiency of 99.79% after 500 cycles and a capacity retention rate of 94.5% at 1.0 C and 25 °C. The composite solid electrolyte (40% PVDF-HFP) can maintain flat and stable stripping/plating plateaus for over 800 hours in symmetrical cells. The amorphous boron nitride nanosheets with high lithium ion conductivity are employed to construct solid-state electrolytes, which is important significant for the development of high energy density, high safety, and long cycle life all-solid-state lithium-ion batteries.

## 1. Introduction

Due to their high energy density, wide temperature range, lack of memory effect, and environmental friendliness, lithium-ion batteries have been widely applied in various fields.<sup>[1]</sup> However, traditional lithium-ion batteries containing liquid organic electrolytes<sup>[2]</sup> usually suffer from flammability, explosiveness, and low energy density,<sup>[3]</sup> is hard to meet the growing market needs of high-power energy storage devices, especially in the development of electric vehicles. Therefore, it is an urgent task to develop new energy storage devices with high energy density and safety.

Solid-state lithium batteries are becoming a hot research field because of their high safety, high energy density, and easily fabrication, and believed to be the "ultimate technology"<sup>[4]</sup> of electrochemical energy storage devices. The

preparation of solid-state electrolytes (SSE) is a critical factor for the development of solid-state batteries.

Currently, solid-state electrolytes are mainly classified as inorganic solid-state electrolytes (ISEs), polymer solid-state electrolytes (SPE), and composite solid-state electrolytes (CSE). The ISEs include Sodium Super Ionic Conductor (NASICON) type,<sup>[5]</sup> garnet type,<sup>[6]</sup> perovskite type,<sup>[7]</sup> and Lithium Super Ionic Conductor (LISICON) type. SPEs<sup>[8]</sup> have polyethylene oxide (PEO),<sup>[9]</sup> polyvinylidene fluoride (PVDF),<sup>[10]</sup> polyacrylonitrile (PAN),<sup>[11]</sup> polymethyl methacrylate (PMMA),<sup>[12]</sup> and poly (vinylidene fluoride-hexafluoropropylene) (PVDF-HFP).<sup>[13]</sup> However, pure ISEs or SPEs are difficult to be used in solid-state batteries individually, due to their respective drawbacks, such as a high interface impedance<sup>[14]</sup> of ISEs, a low room temperature ionic conductivity<sup>[15]</sup> and poor stability of SPEs with lithium metal.<sup>[16]</sup> Therefore, researchers suggest that a composite solid electrolyte<sup>[17]</sup> consisting of inorganic solid-state electrolytes (ISE) and polymer solid-state electrolytes (SPE) should be developed to resolve the issues of solid state batteries.

A high polymer-content composite solid-state electrolyte prepared by adding a small amount of ceramic as an inorganic filler is a typical composite electrolyte.<sup>[18]</sup> Pareek et al.<sup>[19]</sup> incorporated lithium zirconium tin phosphate (LiSnZr (PO<sub>4</sub>)<sub>3</sub>) particles into a polymer matrix (PVDF) with high content to produce a composite electrolyte. Compared to pure polymer solid-state electrolytes ( $2.35 \times 10^{-6} \text{ S cm}^{-1}$ ), the composite electrolyte shows an improved ionic conductivity ( $5.76 \times 10^{-5} \text{ S cm}^{-1}$ ), but it still carries a risk of being penetrated by lithium dendrites.<sup>[20]</sup> When the content of BNNs was 5%, ion conductivity of a solid-state composite electrolyte of boron nitride nanosheets/poly (ethylene glycol) diacrylate (BNNs-

[a] Y. Fang, Y. Yan, X. Wang, S. Lu, B. Liang, Y. Yao, S. Huang, Dr. T. Tao  
School of Materials and Energy, Guangdong University of Technology,  
Guangzhou 510006, P R China  
E-mail: taotao@gdut.edu.cn

[b] D. Q. Tan  
Department of Materials Science and Engineering and Guangdong Provincial Key Laboratory of Materials and Technology for Energy Conversion, Guangdong Technion-Israel Institute of Technology, Shantou 515063, China

[c] Z. Zhang, Dr. T. Tao  
Huizhou Guangdong University of Technology IoT Cooperative Innovation Institute Co., Ltd., Huizhou 516025, China

[d] L. Tian  
Huizhou BTR New Material Technology Co. Ltd., Huizhou 516025, China  
Supporting information for this article is available on the WWW under  
<https://doi.org/10.1002/batt.202400121>

PEGDA) prepared through grafting coupling strategy can reach a maximum of  $1.047 \times 10^{-4} \text{ S cm}^{-1}$ .<sup>[21]</sup> Zhang et al.<sup>[22]</sup> reported the hexagonal boron nitride/polyvinylidene fluoride hexafluoropropylene (h-BN/PVDF-HFP) composite film on SiO<sub>2</sub> substrate using a facile straightforward loading approach, with a room temperature conductivity of  $0.916 \text{ mS cm}^{-1}$ . Therefore, adding high content inorganic fillers to the polymer can further improve the ion conductivity and mechanical properties of the polymer electrolyte, a high ceramic content composite electrolyte<sup>[23]</sup> is developed, which retains both advantages of ceramic electrolytes (high ionic conductivity and Li<sup>+</sup> ion transference number) and polymers (excellent interface compatibility and flexibility). However, developing high ceramic content composite solid electrolytes with high ion conductivity, excellent mechanical strength, and good interface stability remains a challenge.

To address the above issues, two-dimensional amorphous nano boron nitride<sup>[24]</sup> as an inorganic ceramic inert filler in composite solid electrolytes is proposed. In recent years, two-dimensional (2D) nanomaterials have been widely used in electrochemical energy storage. Compared with crystalline boron nitride nano-structures, 2D amorphous boron nitride nanosheets exhibit abundant active sites and surface defects.<sup>[25]</sup> A large specific surface area, excellent insulation, good thermal stability, fast ion migration channels, excellent thermal expansion coefficient and thermal conductivity, is conducive to increasing charge storage active sites and mechanical strength of 2D amorphous boron nitride nanosheets, thereby enhancing their adhesion and ultimately improving the energy storage of batteries. The amorphous nature and 2D structure with synergistic effects often result in excellent energy storage and mechanical performance. Novoselov et al.<sup>[26]</sup> initially utilized the mechanical exfoliation method to extract single-layer graphene nanosheets from graphite. Coleman et al.<sup>[27]</sup> successfully prepared graphene from graphite by liquid-phase exfoliation. Oh B. Chae et al.<sup>[28]</sup> prepared two-dimensional amorphous V<sub>2</sub>O<sub>5</sub> nanomaterials as the cathode in lithium-ion batteries via precipitation method, exhibiting a higher discharge specific capacity than that of its crystalline counterpart. Sun and his colleagues<sup>[29]</sup> prepared two-dimensional amorphous FeO<sub>x</sub> nanosheets as the anode for sodium-ion batteries using a chemical synthesis method, which showed a capacity remains at  $214.4 \text{ mAh g}^{-1}$  after 500 cycles at  $1 \text{ A g}^{-1}$ . Zhao et al.<sup>[30]</sup> demonstrated excellent performance of amorphous Cr<sub>2</sub>O<sub>3</sub> nanosheets, synthesized using a stripping method, as the anode in lithium-ion batteries.

Researchers<sup>[31]</sup> have also prepared few-layer BN nanomaterials using a ball-milling exfoliation method. Deng et al.<sup>[32]</sup> successfully prepared a large amount of amorphous BN nanosheets using a ball-milling combined with water washing exfoliation method, exhibiting good mechanical properties,<sup>[33]</sup> high thermal and chemistry stability, excellent electrical insulation,<sup>[34]</sup> and high thermal conductivity. The amorphous boron nitride prepared by ball milling shows many defects.<sup>[35]</sup> The ultra-thin amorphous BN dielectric films reported by Glavin et al.<sup>[36]</sup> to be applied to capacitor equipment. A 3 nm thick amorphous boron nitride thin layer obtained by low-temperature remote inductively coupled plasma chemical vapor deposition (ICP-CVD) method,<sup>[34]</sup> which exhibits ultra-low dielec-

tric properties up to 1.16 at a working frequency of 1 MHz. The thin film exhibits a strong mechanical and high-pressure stability, which is beneficial for applications in the field of electrochemical energy storage.

Here, the amorphous BN nanosheets are employed as a matrix to fabricate a flexible high-ceramic-content amorphous BN nanosheets/PVDF-HFP composite solid electrolyte by a simple solution casting method. Two-dimensional amorphous boron nitride nanosheet belongs to inert ceramic fillers. The obtained amorphous BN nanosheets/PVDF-HFP (40%) composite exhibits a good interface compatibility, high ionic conductivity ( $1.936 \times 10^{-3} \text{ S cm}^{-1}$  at  $25^\circ\text{C}$ ) and electronic insulation, and excellent thermal and electrochemical stability, significantly reducing interface resistance and increasing the Li<sup>+</sup> conductivity of all solid state lithium batteries.

## 2. Results and Discussion

The original h-BN with layered structure can be completely transformed into the amorphous BN nanosheets by ball milling insertion and pure water exfoliation method, as shown in Figure 1 (a-d). After cold pressing, a solid state electrolyte film of pure h-BN particles (Figure 1e) and a solid state electrolyte film of pure amorphous BN nanosheets (Figure 1f) are obtained, respectively, indicating a good film-forming of pure h-BN particles and amorphous BN nanosheets. A composite solid state electrolyte film composed of h-BN particles and PVDF-HFP (40%) (Figure 1g, h) and a composite solid state electrolyte film composed of amorphous BN nanosheets and PVDF-HFP (40%) (Figure 1i, j) are prepared by a simple solution-casting method, demonstrating that h-BN particles or amorphous BN nanosheets and PVDF-HFP (40%) have a good compatibility. In comparison with h-BN/PVDF-HFP and SPE (Figure S1(a-b)), no obvious particle agglomeration and pores are found on the surface of the obtained amorphous BN nanosheets based composite films. All the surface of BN-based films are smooth, uniform and denser. After folding, the amorphous BN nanosheets based composite film does not crack, and no any significant deformation can be detected (Figure 1k, l), revealing that the prepared amorphous BN nanosheets/PVDF-HFP composite electrolyte has a good structural integrity and flexibility. Its thickness is about 200  $\mu\text{m}$ , and each elements inculding C (representing the polymer), F, B (representing BN), and S (representing LiTFSI) is uniform distribution in the CSE (Figure 1 (n-q)), indicating that both amorphous BN nanosheets and PVDF-HFP are mutually compatible.

The color change of the resulted films is clear from white to transparent (Figure 2a), with the increase of PVDF-HFP content (CSE-x ( $x=0, 20\%, 30\%, 40\%, 50\%, 70\%, 100\%$ )). In order to confirm the chemical stability of amorphous BN nanosheets, the obtained products are characterized by X-ray diffraction (XRD) (Figure 2b). No obvious h-BN diffraction peaks are found in the amorphous BN nanosheets and their composite solid state electrolyte films. The ion conductivities of these films are also evaluated and calculated, as shown in Figure 2c and Table 1, The obtained batteries are named as SS/ amorphous BN-LiTFSI

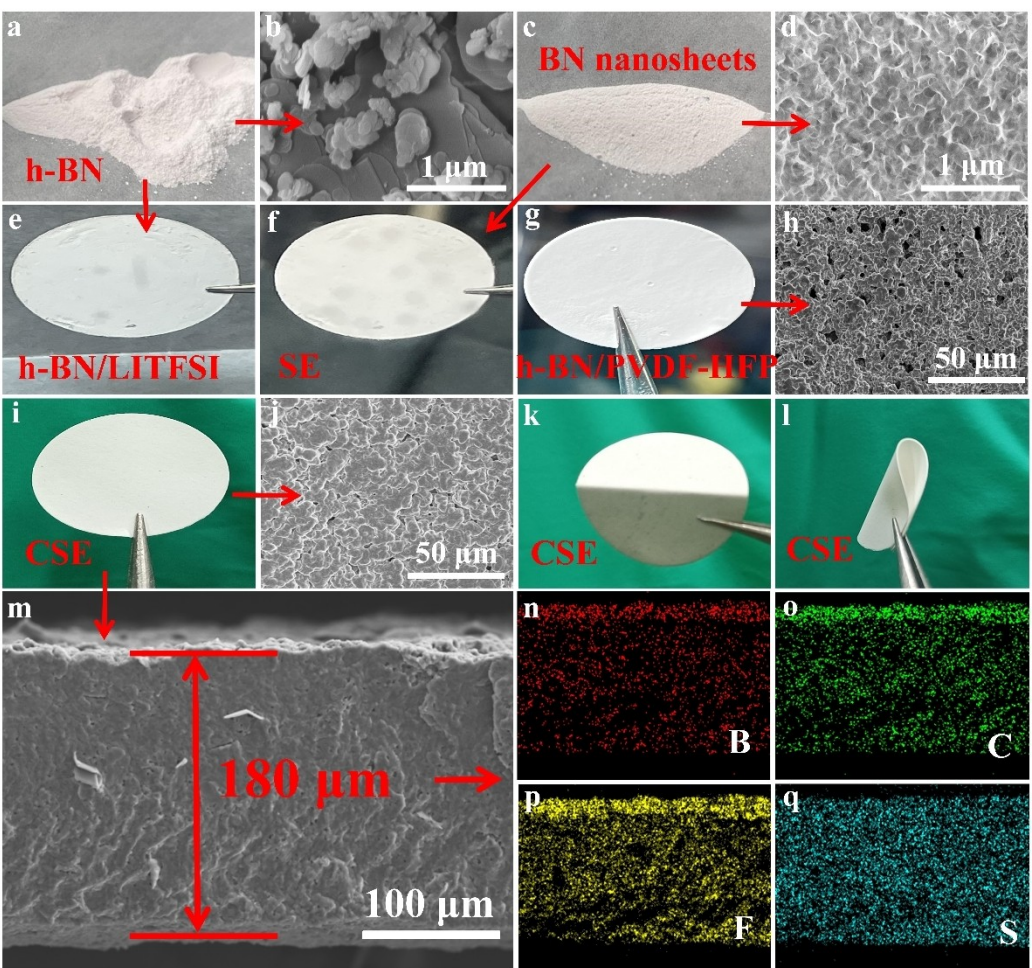


**Figure 1.** a, b) Optical and SEM images of h-BN particles; c, d) Optical and SEM images of amorphous BN nanosheets; e, f) Optical images of h-BN/LiTFSI and SE films formed by cold pressing, respectively; g, h) Optical and SEM images of h-BN/PVDF-HFP; i, j) Optical images of the CSE film, respectively; k, l) Optical images of the folded and bent CSE film; m) Cross-sectional SEM image of the CSE membrane; and n–q) EDS image of the distribution of B, C, F, and S elements in the CSE film.

(SE)/SS, SS/PVDF-HFP-LiTFSI (SPE)/SS, SS/h-BN-PVDF-HFP/SS and SS/amorphous BN-LiTFSI-xPVDF-HFP (CSE-x,  $x=20\%, 30\%, 40\%, 50\%, 70\%$ )/SS, respectively. Among them, the composite electrolyte with 40% PVDF-HFP (CSE-40%) exhibits the highest ion conductivity of  $1.936 \times 10^{-3} \text{ Scm}^{-1}$ , which is approximately 20 times that of the SPE and much higher than that of the h-BN/PVDF-HFP ( $0.429 \times 10^{-3} \text{ Scm}^{-1}$ ). The high ion conductivity could be attributed to the unique structure of amorphous BN nanosheets with a high specific surface area and a large number of Lewis acid-base interaction sites, promoting the dissociation of lithium salts and providing fast channels for  $\text{Li}^+$  transport.<sup>[18,37]</sup> While the content of PVDF-HFP in composite electrolyte exceeds 40%, the conductivity decreases, revealing that adding excessive PVDF-HFP or amorphous nanosheets may be not

conducive to the synergistic effect of amorphous BN nanosheets and polymers, increasing the crystallization zone or disperse inorganic fillers, which will reduce the migration rate of lithium ions.

To evaluate the electrochemical stability window of solid electrolytes, LSV measurements were conducted. As shown in Figure 2d, it is observed that the decomposition voltage of CSE-40% is 5 V, which is higher than that of SE, SPE, h-BN/PVDF-HFP and CSE-x ( $x=20\%, 30\%, 50\%, 70\%$ ). This is due to the inherent high chemical and electrochemical stability of amorphous BN nanosheets. The B atoms in amorphous BN nanosheets can bind to the electrons on the O atoms of the  $\text{TFSI}^-$  anions, resulting in the adsorption of the entire anion on the surface of the amorphous BN nanosheets, and alleviating the

**Table 1.** Ionic conductivity of composite solid electrolyte CSE with various PVDF-HFP contents.

Content of PVDF (%)	SE(0)	20	30	40	50	70	SPE(100)
Ionic conductivity ( $10^{-3}$ )	0.403	1.14	1.187	1.936	0.443	0.208	0.095

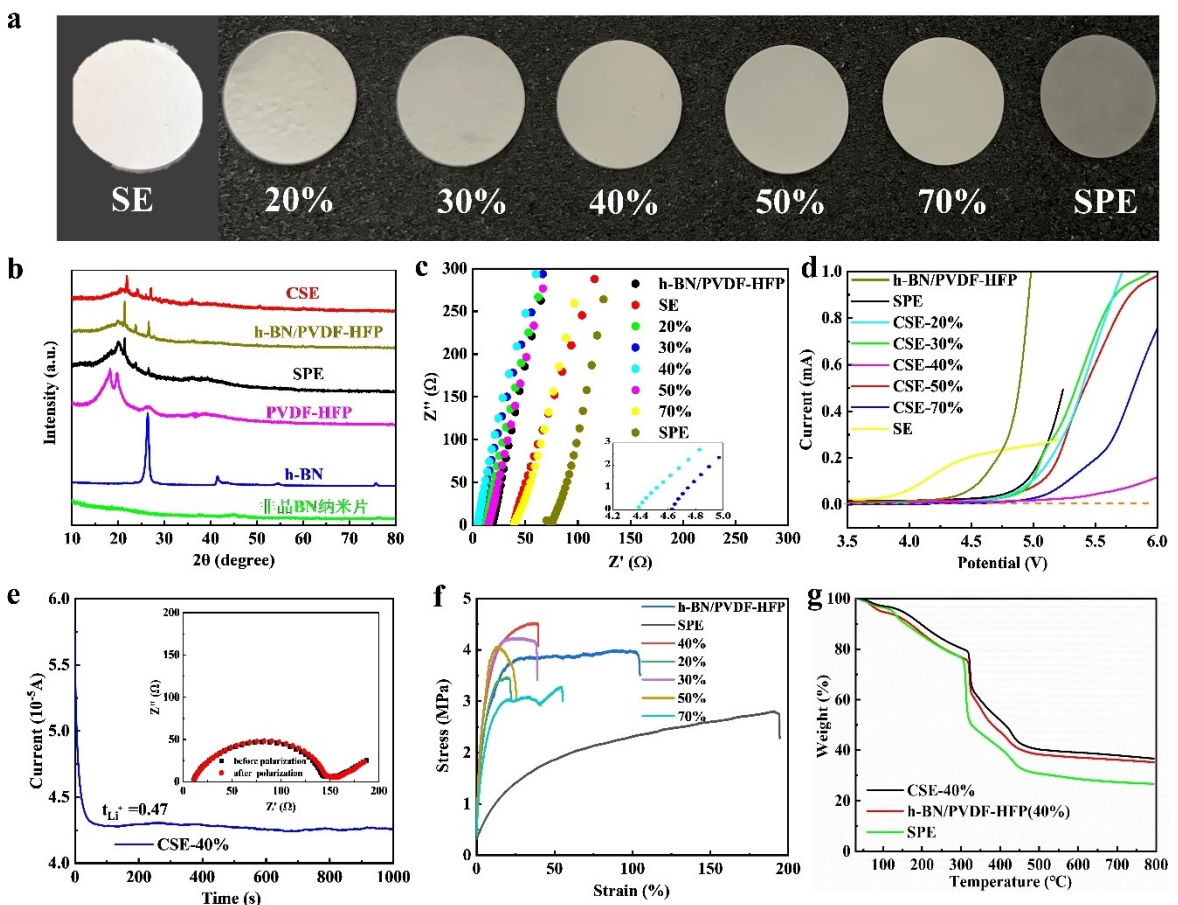


**Figure 2.** a) Optical images of SE, SPE, and CSE- $x$  ( $x = 20\%, 30\%, 40\%, 50\%, 70\%$ ) membranes, respectively; b) XRD patterns of h-BN, amorphous BN nanosheets, PVDF-HFP, h-BN/PVDF-HFP, SPE, and CSE-40%; c) EIS curves of SS/SE/SS, SS/SPE/SS, SS/h-BN/PVDF-HFP/SS, and SS/CSE- $x$  ( $x = 20\%, 30\%, 40\%, 50\%, 70\%$ )/SS; d) LSV curves of SS/SE/Li, SS/h-BN/PVDF-HFP/Li, SS/SPE/Li, and SS/CSE- $x$  ( $x = 20\%, 30\%, 40\%, 50\%, 70\%$ )/Li; e) Steady-state polarization and impedance curves of Li/CSE-40%/Li before and after polarization; f) Stress-strain, and g) thermal gravimetric curves of CSE-40%, SPE, and h-BN/PVDF-HFP (40%).

decomposition of the polymer electrolyte.<sup>[38]</sup> Figure 2e shows the steady state polarization curve and the impedance of the Li/CSE-40%/Li cells before and after polarization, and its corresponding Li<sup>+</sup> transference numbers ( $t_{Li^+}$ ) are calculated (0.47), which is higher than that of SE (0.26), SPE (0.15), h-BN/PVDF-HFP (0.4) are shown in Figure S2a. Attributed to the that boron (B) atoms on the surface of amorphous BN nanosheets with a larger specific surface area bind with oxygen (O) atoms in TFSI anions, hindering the movement of anions, while prompting the rapid transport<sup>[39]</sup> of Li<sup>+</sup> along the surface of amorphous BN nanosheets, therefore increasing the migration number of lithium ions.

The stress-strain curves for SPE, CSE- $x$  ( $x = 20\%, 30\%, 40\%, 50\%, 70\%$ ), h-BN/PVDF-HFP (40%) membrane are shown in Figure 2f, respectively. Due to the strong planar covalent bonds generated from amorphous BN nanosheets,<sup>[40]</sup> CSE-40% has a maximum tensile strength (4.525 MPa), which is significantly higher than that of h-BN/PVDF-HFP (3.987 MPa) and SPE (2.806 MPa). When the ratio of amorphous BN to PVDF-HFP is 1 g: 0.8 g, the composite electrolyte exhibits the higher ion conductivity, wider electrochemical stability window (5 V),

better mechanical strength (4.525 MPa), and higher lithium ion transference number (0.47).

To reveal the thermal stability of solid electrolytes, thermogravimetric analysis (TG) is performed. As shown in Figure 2g, the thermal decomposition temperature of CSE-40% (320 °C) is the higher, while h-BN/PVDF-HFP and SPE are 318 °C and 308 °C, respectively. This indicates that the BN ceramic filler contributes to enhance the thermal stability of polymer-based composite electrolytes. Furthermore, compared to the h-BN/PVDF-HFP composite film, the thermal decomposition rate of the amorphous BN nanosheets composite film is slower, suggesting that the thermal stability of amorphous BN nanosheets is better than that of the crystalline BN. The DSC curves of SPE and CSE-40% samples are shown in Figure S2b. It can be seen that after adding amorphous BN nanosheets, the thermal transition temperature shifts towards lower temperatures, indicating that the addition of amorphous BN nanosheets can reduce the crystallization zone of the polymer.

In order to further evaluate the thermal stability of the electrolyte, a heat shrinkage experiment is conducted, as shown in Figure 3a. The CSE-40% film exhibits a slight shrinkage from 25 °C to 250 °C, while the PP separator and SPE are melting/

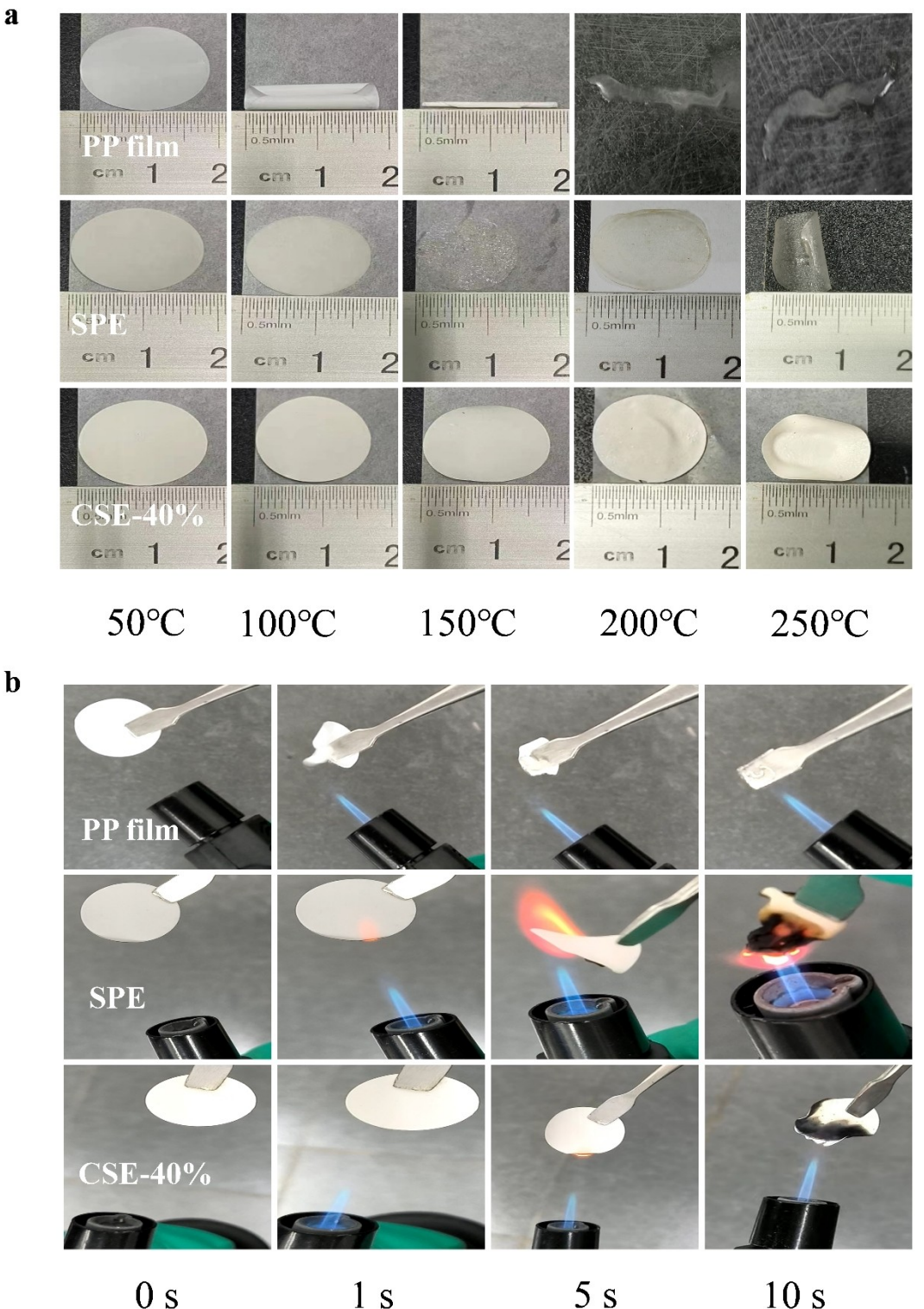


**Figure 3.** a) Thermal shrinkage tests of at various temperatures of 50 °C, 100 °C, 150 °C, 200 °C, and 250 °C; and b) flame retardant performance testing for PP membrane, SPE, and CSE-40%.

severe curling and partial melting, respectively, at 250 °C. Figure 3b shows the flame retardancy test of PP membrane, SPE, and CSE-40%. The PP membrane is rapidly burned instantaneously, the SPE burns intensively and undergoes an irreversible deformation, while CSE-40% shows an excellent

flame retardancy and high thermal stability, which is heated in a pure gas flame for 10 second and the charred amorphous BN nanosheets based composite film still maintains a semicircle shape.

Compared with other composite solid electrolytes, amorphous BN nanosheets/LiTFSI/PVDF-HFP with high ceramic content and high ionic conductivity exhibit better electrochemical performance. This is mainly attributed to the large specific surface area provided by amorphous BN nanosheets, which have Lewis acid-base interaction sites, can fix anions, promote lithium salt dissociation, reduce polymer crystallinity, and improve the movement of lithium ions in the electrolyte. The specific structure of two-dimensional amorphous BN nano-

sheets may also hinder the transport of lithium ions, thereby increasing ion transport pathways.

The cyclic voltammetry (CV) curves of LFP/CSE-40% Li cells (Figure 4a) at room temperature show that, both the oxidation peaks and the reduction peaks do not significantly shift after several cycles, indicating a good reversibility of CSE. To reveal the interface stability between the lithium metal anode and solid electrolyte, the constant current cycling performance of the Li/CSE-40% Li symmetrical cell is tested, as shown in

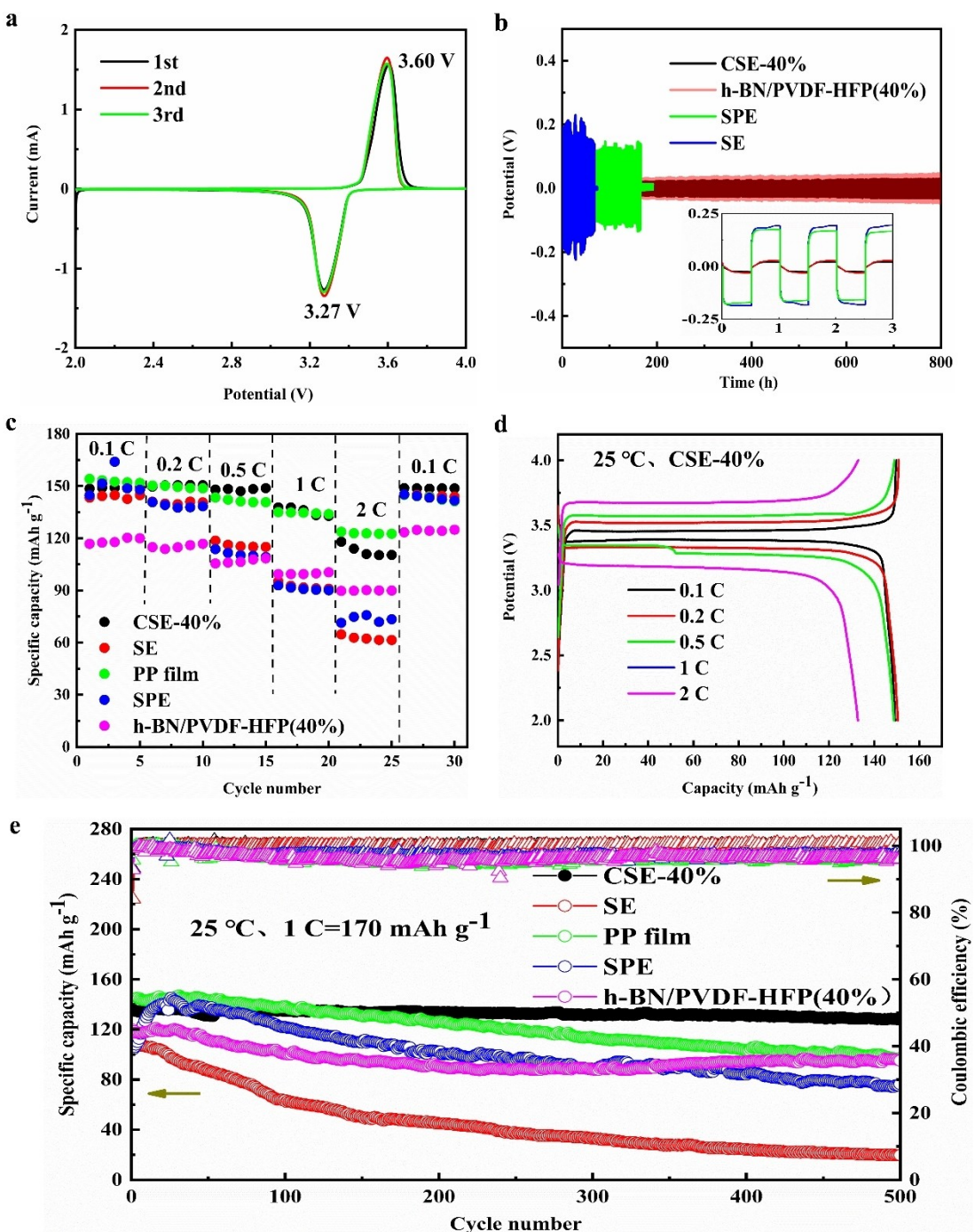


**Figure 4.** a) CV curves of LFP/CSE-40% Li cell; b) lithium deposition/stripping cycle tests of Li/CSE-40% Li, Li/SE/Li, Li/SPE/Li, and Li/ (h-BN/PVDF-HFP (40%)) /Li symmetrical cells; c) rate performances and e) cycle performances for LFP/SSE/Li cells with CSE-40%, SE, PP membrane, SPE and h-BN/PVDF-HFP (40%), respectively; and d) charge-discharge curves at different rates.

Figure 4b. It demonstrates that the CSE-40% battery containing amorphous BN nanosheets exhibits a stable voltage distribution over 800 hours without noticeable polarization or short-circuit phenomena. In contrast, the SE and SPE batteries experience significant polarization short-circuit after cycling for 68 hours and 166 hours. It is found that the disassembled lithium anode of the CSE-40% battery still keeps the smooth and flat surface after cycling (Figure S1(c-d)), indicating that lithium dendrites do not form during the charging and discharging process. These results indicate that CSE-40% can effectively suppress lithium dendrite growth and reduces the risk of battery short-circuits caused by lithium dendrites.

Although batteries containing liquid electrolyte and PP separators can achieve the high initial capacity of  $154.1 \text{ mAh g}^{-1}$  at 0.1 C ( $1 \text{ C} = 170 \text{ mAh g}^{-1}$ ) at room temperature, they only sustain  $144.9 \text{ mAh g}^{-1}$  when returning from 2 C to 0.1 C, as shown in Figure 4c. At the current densities of 0.1 C, 0.2 C, 0.5 C, 1 C, and 2 C, the discharge specific capacity of the CSE-40% based solid-state battery is  $148.5 \text{ mAh g}^{-1}$ ,  $149.7 \text{ mAh g}^{-1}$ ,  $148.0 \text{ mAh g}^{-1}$ ,  $137.7 \text{ mAh g}^{-1}$ , and  $118.0 \text{ mAh g}^{-1}$  respectively. When returned to 0.1 C, its discharge specific capacity can be restored to  $148.8 \text{ mAh g}^{-1}$ . Compared to SE, PP separators, SPE, h-BN-PVDF-HFP (40%), and CSE-20%, 30%, 50% or 70% (Figure S3a-b), the LFP/Li battery assembled with 40% CSE electrolyte exhibits a superior reversibility and electrochemical performance. Figure 4d displays the charge-discharge curves of the CSE-40%-based solid-state battery at various current density, showing the typical charge and discharge plateau of LiFePO<sub>4</sub> electrodes. With the increase of current density, the discharge capacity of the battery decreases, from  $148.5 \text{ mAh g}^{-1}$  at 0.1 C to  $118 \text{ mAh g}^{-1}$  at 2 C, due to the electrode polarization caused by rapid voltage increase or decrease.

To further investigate the electrochemical performance of the CSE, the ambient temperature cycling performance is illustrated in Figure 4e. The initial discharge capacity of LFP/CSE-40%/Li is  $135.6 \text{ mAh g}^{-1}$  at 1 C, and its reversible capacity remains at  $128.1 \text{ mAh g}^{-1}$ , Coulombic efficiency is 99.79% and a capacity retention 94.5% after 500 charge/discharge cycles. While the cells with SE, PP separator, SPE, and h-BN-PVDF-HFP (40%) only exhibit the discharge specific capacities of  $19.7 \text{ mAh g}^{-1}$ ,  $97.3 \text{ mAh g}^{-1}$ ,  $76.5 \text{ mAh g}^{-1}$ , and  $75.2 \text{ mAh g}^{-1}$  after 500 cycles, and their capacity retentions are 18.2%, 67.2%, 73.3%, and 79.5%, respectively. These results clearly indicate that CSE-40% significantly enhances the cycling performance of solid state batteries. Additionally, the charge/discharge curves for CSE-40% at various cycle numbers are shown in Figure S3c, and a slight increase in polarization voltage is observed during prolonged cycling, indicating the good interface stability of CSE-40% based cells.

Figure 5a shows the CV curve of the NCM811/CSE-40%/Li cell at a scanning speed of  $0.1 \text{ mV s}^{-1}$ , which is consistent with the typical CV curve of the traditional NCM811-based lithium batteries. Figure 5b illustrates the rate performance of NCM811/CSE-40%/Li, NCM811/PP separator/Li, and NCM811/SPE/Li cells at room temperature, respectively. It is observed that the NCM811/CSE-40%/Li cell can maintain the discharge specific capacities of  $194.7 \text{ mAh g}^{-1}$ ,  $184.5 \text{ mAh g}^{-1}$ ,  $167.5 \text{ mAh g}^{-1}$ ,

$141.9 \text{ mAh g}^{-1}$ , and  $127.6 \text{ mAh g}^{-1}$  at current densities of 0.1 C, 0.25 C, 0.5 C, 1 C, and 1.5 C ( $1 \text{ C} = 200 \text{ mAh g}^{-1}$ ), respectively. Upon returning to 0.1 C, the discharge specific capacity is able to recover to its initial level, demonstrating its good reversibility. The cycling performance of NCM811/CSE-40%/Li, NCM811/PP separator/Li, NCM811/SPE/Li, and NCM811/SE/Li are shown in Figure 5c. Among them, CSE-40% exhibits a higher initial discharge capacity of  $170.5 \text{ mAh g}^{-1}$  and a capacity retention of 83.3% after 1 C and 100 cycles. This indicates that the CSE-40% electrolyte can maintain a good stability under prolonged high voltage and a high coulombic efficiency close to 98%. Figure 5d shows the charge-discharge curves of the 20th cycle for various cells. The charge-discharge plateaus of CSE-40% based cell exhibit the low polarization voltage, indicating the stable interface between the electrolyte and the electrode during cycling. The selected charge-discharge curves of NCM811/CSE-40%/Li for the 20th cycle are shown in Figure 5e. All the charge-discharge platforms align with the charge-discharge platform of typical NCM811 based cell, exhibiting the small polarization voltage and the excellent stability of the CSE-40%/electrode interface.

After 500 cycles, the LFP/CSE-40%/Li based cell is disassembled in the glovebox. It is found that the lithium metal anode, CSE-40% based solid state electrolyte, and cathode are still tightly integrated, and the architecture of the cell is intact (Figures 6a and 6c). After scraping off the cathode, residual cathode materials adhere on the surface of CSE-40% based film (Figure 6b and e). While the lithium metal anode is easily stripped from the film, relatively (Figure 6d). No damage occurs for CSE-40% based solid state electrolyte film during installation, charge-discharge and disassembly process, and the surface of both anode and cathode sides is compact and flat throughout the whole process (Figure 6f-h). These results confirm the excellent interface compatibility and mechanical behavior, and outstanding electrochemical cycling stability of the CSE-40% based solid state electrolyte.

Figures 6i-j show the models of Li<sup>+</sup> and TFSI<sup>-</sup> adsorption on BN nanosheets and amorphous BN, respectively. The calculated results are presented in Table 2. It can be observed that the adsorption energies of Li<sup>+</sup> and TFSI<sup>-</sup> on the crystalline BN nanosheets are 1.64 eV and 2.187 eV, respectively, while on the amorphous BN nanosheets, they are 4.299 eV and 7.508 eV, respectively. The surface of BN exhibits stronger adsorption for anions, compared to lithium ions, which enhances the transference of lithium ions during the conduction process. Additionally, the adsorption energy of amorphous BN is greater than that of crystalline BN, confirming a higher lithium ion conductivity of amorphous BN nanosheets than that of crystalline BN nanosheets.

### 3. Conclusions

In conclusion, we have designed and prepared a solid state composite electrolyte based amorphous BN nanosheets and PVDF-HFP. Amorphous BN nanosheets have excellent insulation properties and electrochemical stability. We demonstrate that

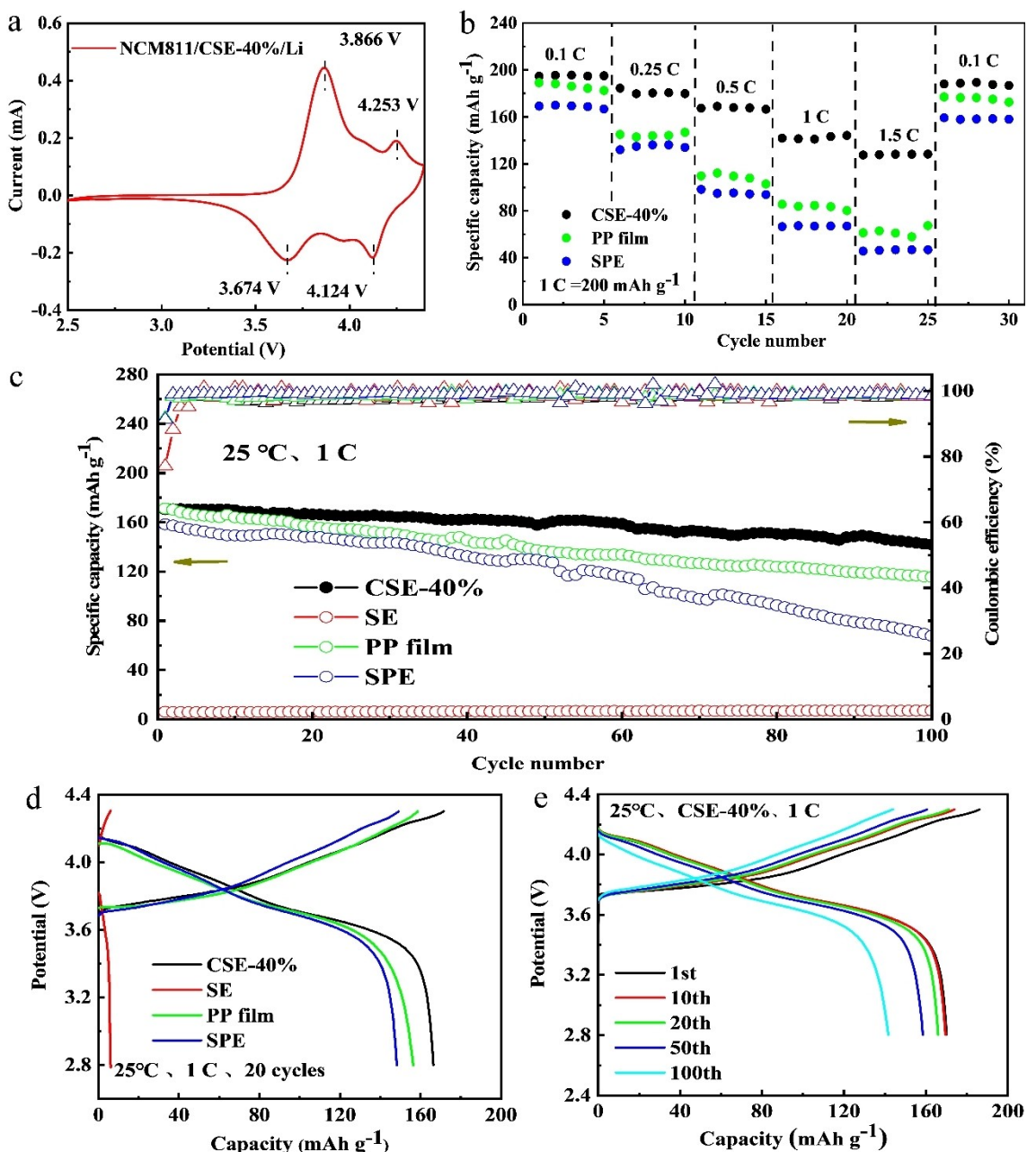


**Figure 5.** a) CV curves of NCM811/CSE-40%/Li cell; b) rate performance and c) cycle performance for LFP/SSE/Li cells with CSE-40%, SE, PP membrane, SPE, and h-BN/PVDF-HPF(40%), respectively; d) charge-discharge curves of various electrolytes at the 20th cycle; and e) charge-discharge curves of NCM811/CSE-40%/Li cells at 200 mAh g<sup>-1</sup> and 25 °C.

the prepared composite electrolyte can maintain a high ionic conductivity, and ensure an excellent mechanical performance and interface compatibility. This composite solid-state electro-

lyte exhibits exceptional electrochemical performance, particularly CSE-40% based electrolyte displays a wide electrochemical stability window (5 V), moderate lithium ion transference

**Table 2.** The adsorption capability of the crystalline/amorphous BN nanosheets for TFSI<sup>-</sup> and Li<sup>+</sup> ions.

Type Structure	Type of substance	Total(eV)	Sur-BN(eV)	Li/TFSI(eV)	AD(eV)
Crystal BN nanosheets	Li	-809.839	-807.887	-0.307	-1.644
	TFSI	-891.622	-807.910	-81.525	-2.187
Amorphous BN nanosheets	Li	-738.022	-733.420	-0.303	-4.299
	TFSI	-818.974	-730.291	-81.174	-7.508

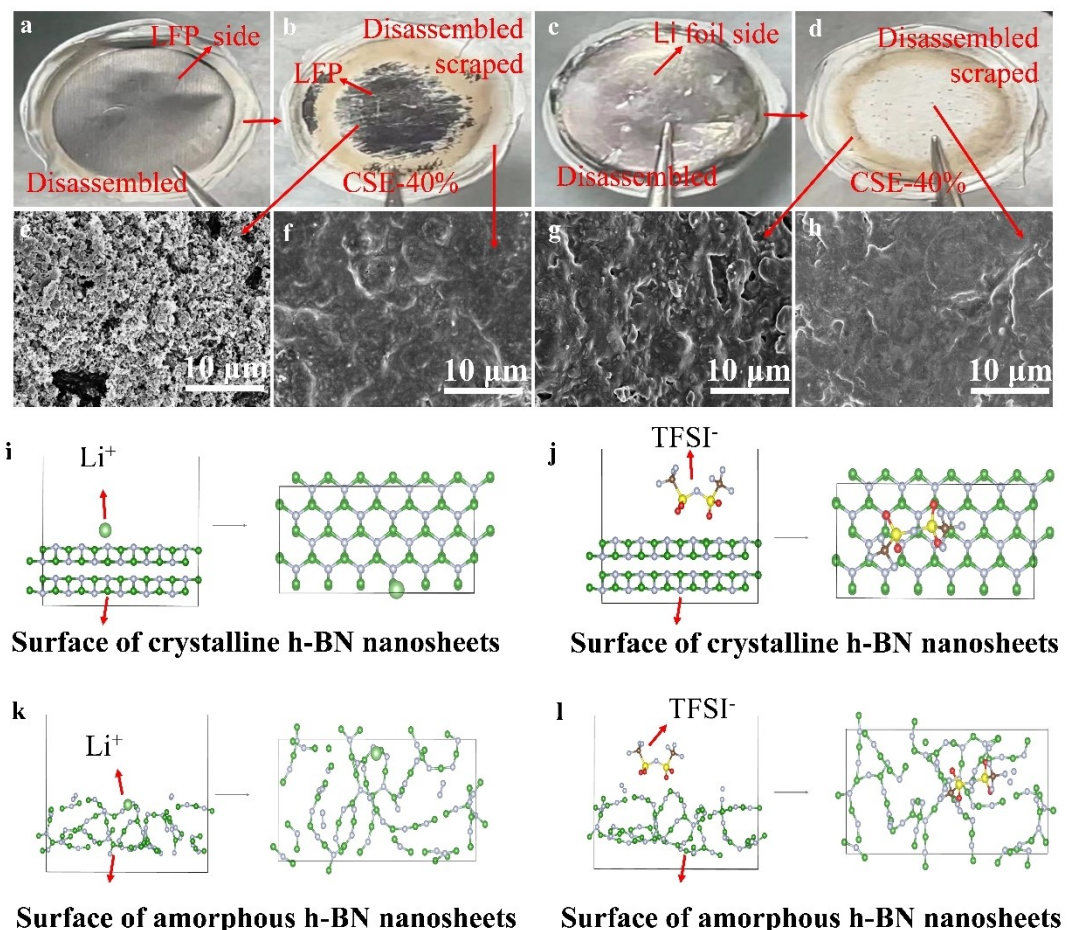


**Figure 6.** a and c) optical images of anode and cathode sides for LFP/CSE-40%/Li based battery disassembled after 500 cycles, respectively; b and e) optical and SEM images of the residual cathode material adhering to the CSE-40% film after scraping off, respectively; d) optical image of the film peeling off lithium metal anode; f-h) SEM images of CSE-40% film surface scraping off the cathode and anode after 500 cycles; i) Li<sup>+</sup> adsorption model on crystalline BN nanosheets; j) TFSI<sup>-</sup> adsorption model on crystalline BN nanosheets; k) Li<sup>+</sup> adsorption model on amorphous BN nanosheets; and l) TFSI<sup>-</sup> adsorption model on amorphous BN nanosheets.

number (0.47), and high ionic conductivity ( $1.936 \times 10^{-3} \text{ S cm}^{-1}$ ). The solid-state battery constructed by this composite delivers a high capacity of  $128.1 \text{ mAh g}^{-1}$  and retains 94.5% of its original capacity after 500 charge-discharge cycles in a LiFePO<sub>4</sub>/Li full solid-state battery. The theoretical calculations show that the B atoms on the surface of amorphous BN nanosheets show a high adsorption energy towards O atoms in TFSI, providing numerous Lewis acid-base sites to facilitate lithium salt dissociation and thus ensuring high ionic conductivity of the electrolyte.

## Experimental Section

**Preparation of amorphous BN Nanosheets:** a mixture of 1 g h-BN and 100 g different diameter zirconia balls (including 3 mm (20 g), 5 mm (30 g), 8 mm (30 g), 10 mm (20 g)) was placed in a zirconia ball milling tank and dried at  $100^\circ\text{C}$  for 2 hours in an oven. Then, the tank was transferred to a glovebox (water and oxygen content lower than 0.1 ppm) for a 2 hours vacuum treatment to remove the residual air, and added into small pieces of lithium metal produced by uniformly cutting lithium foils. Adding several pieces of lithium metal are used to exfoliate the layered BN to prepare amorphous

BN nanosheets by a violent solid-state reaction. Lithium metal atoms can be inserted into the interlayer of h-BN, and amorphous BN nanosheets are prepared by solid-state intercalation and pure water exfoliation. The mixture of lithium foils and h-BN was ball milled at room temperature, under argon atmosphere, and at 350 rpm using a Pulverisette 5 ball mill for 36 hours. After ball milling, 40 mg of the ball-milled composite powder were taken and placed in a beaker (300 mL), and 200 mL of deionized water at  $60^\circ\text{C}$  were immediately poured into the beaker. After stirring for 30 minutes to form a homogeneous suspension, and then filtered, and the resulting solid sample was dried at  $60^\circ\text{C}$  for 12 hours. The preparation process of amorphous BN nanosheets was described elsewhere in detail.<sup>[32]</sup>

Hexagonal boron nitride (h-BN) and polyvinylidene hexa-fluoropropylene copolymer (PVDF-HFP, MW=400,000) were purchased from Macklin. Lithium bis (trifluoromethanesulfonyl) imide (LiTFSI), N,N-dimethylformamide (99.5%), and anhydrous acetonitrile (99.9%) were procured from Aladdin. Lithium lanthanum zirconium titanate (LLZTO) was purchased from Hefei Kejing Materials Technology Co., Ltd. Other battery materials such as LiFePO<sub>4</sub> (LFP) powder, NCM811 powder, conductive carbon black (Super P), Polypropylene (PP) membrane and lithium foil, were purchased from Kelude Experimental Equipment Technology Co., Ltd.

**Preparation of amorphous BN nanosheets/PVDF-HFP composite solid-state electrolyte:** Initially, 1 g amorphous BN nanosheets and 1 g LiTFSI (in a 1:1 weight ratio) were poured into a glass container, and adding 45 mL of N,N-dimethylformamide solvent to form a mixture in the glovebox. To optimize the proportion, the mixture with different contents of PVDF-HFP were prepared respectively, including PVDF-HFP content of 20%, 30%, 40%, 50%, and 70%, namely 0.4 g, 0.6 g, 0.8 g, 1.0 g, and 1.4 g (in relation to the total amount of amorphous BN nanosheets and LiTFSI). Then the container was sealed with a plastic film and stirred at 55 °C in the glovebox for 24 hours. After stirring, the mixture was transferred from the glovebox, poured into a polytetrafluoroethylene mold, and placed in a vacuum oven at 55 °C for 36 hours. Then, the mold was transferred immediately to the glovebox antechamber and naturally cooled under vacuum for 2 hours to remove residual solvent before sealing in the glovebox for storage.

To compare with amorphous BN nanosheets, the following electrolytes were prepared respectively: a commercial h-BN/PVDF-HFP (40%) composite electrolyte (1 g h-BN, 1 g LiTFSI, 0.8 g PVDF-HFP); LLZTO/PVDF-HFP (40%) composite electrolyte (1 g, LLZTO, 1 g LiTFSI, 0.8 g PVDF-HFP); PVDF-HFP/LiTFSI polymer electrolyte referred to as SPE (2 g PVDF-HFP, 1 g LiTFSI); and amorphous BN nanosheets /LiTFSI inorganic electrolyte referred to as SE (1 g amorphous BN nanosheets and 1 g LiTFSI). The formation process of amorphous BN nanosheets /LiTFSI inorganic electrolyte film differs from that of composite solid-state electrolytes, which was formed by pressing, while the composite solid-state electrolytes formed by casting. The amorphous BN nanosheets were mixed with LiTFSI in a 1:1 ratio, added to an appropriate amount of anhydrous acetonitrile, and stirred at room temperature for 24 hours. Then, the mixture was dried at 100 °C in an oven and immediately transferred to a glove box, ground for 30 minutes, and stored in a sealed container. 80–120 mg of amorphous BN nanosheets/LiTFSI powder were pressed at 100 MPa for 2 minutes in a stainless steel mold to produce a 15 mm diameter film.

**Characterization:** The surface and cross-sectional morphology and elemental distribution of the solid electrolyte were observed using a scanning electron microscope (SEM, Hitachi Co., SU8220) and energy-dispersive spectroscopy (EDS) respectively. X-ray diffraction analysis (XRD, Ultima-IV) was performed in the 10–80° range at a scanning rate of 10° min<sup>-1</sup>. The mechanical strength of the solid electrolyte was studied using a high/low-temperature universal testing machine (Inpekt Table Blue 5 KN) with a tensile rate of 5 mm min<sup>-1</sup>. The decomposition temperature of the solid electrolyte in a nitrogen atmosphere was investigated using a thermal gravimetric analyzer (TGA, SDT Q600) in the temperature range of 30–800 °C at a heating rate of 10 °C min<sup>-1</sup>.

Samples of PP membrane, SPE, and CSE-40% were cut into circular shapes with a diameter of 19 mm for testing the thermal stability in an oven. To observe the shrinkage of the solid-state electrolytes at different temperatures, the films were continuously heated and maintained for 30 minutes at a series of temperatures of 50 °C, 100 °C, 150 °C, 200 °C, and 250 °C. Also, the flame retardancy testing of the films was performed, and the morphology change process was recorded after 1 s, 3 s, 5 s, and 10 s of burning.

The electrochemical workstation (CHI660E) was used to conduct cyclic voltammetry (CV), electrochemical impedance spectroscopy (EIS), linear sweep voltammetry (LSV), and chronoamperometry (i-t) tests. The scan rate for CV was 0.1 mV s<sup>-1</sup>. The ionic conductivity of the solid electrolyte was evaluated by stainless steel plate (SS)/CSE/SS block cells. EIS was conducted to test the conductivity of Li<sup>+</sup> in a frequency range of 10<sup>-1</sup> Hz–10<sup>6</sup> Hz, using an AC signal amplitude of 5 mV at a temperature of 25 °C. Ionic conductivity was calculated through equations  $\sigma = L/R_b S$ , where L is the thickness of the solid

electrolyte, R<sub>b</sub> is the body impedance of the solid electrolyte, S is the area of the contact portion of the solid electrolyte and the SS. The SS/CSE/Li cells were used for linear sweep voltammetry (LSV) measurement at a scanning speed of 0.01 V s<sup>-1</sup> in the range of 3.5–6 V (vs. Li<sup>+</sup>/Li). The Li/SE/Li symmetric cells were assembled by sandwiching two pieces of Li plates and a piece of solid electrolyte. The ion transference number was calculated by the formula  $t_{Li^+} = [I_s \times (\Delta V - I_o R_o)] / [I_o \times (\Delta V - I_s R_s)]$ .  $\Delta V$  is the applied voltage (10 mV), I<sub>o</sub> and I<sub>s</sub> are the initial and stable currents, R<sub>o</sub> and R<sub>s</sub> are the electrode/electrolyte interface resistance before and after polarization which were fitted by Zview software, respectively. Density functional theory (DFT) calculations were performed on the adsorption energies of anionic cations in crystalline h-BN and amorphous BN nanosheets with LiTFSI to investigate their interactions. The calculation formula is  $E_{ads} = E_{total} - E_{sur} - E_m$ , E<sub>total</sub> represents the total energy of the adsorption system, while E<sub>sur</sub> and E<sub>m</sub> respectively denote the energies of the surface and detached Li atoms and TFSI molecules.

Two types of composite positive electrodes were prepared in a glovebox filled with argon. The positive electrode formulation is consisted of LFP or NCM811, PVDF binder, and Super-P in a mass ratio of 7:2:1. The negative electrode was composed of lithium foil. The stability of the lithium metal-CSE interface was evaluated through constant current cyclic tests of a symmetrical Li/CSE/Li cell. The testing current density was set at 0.1 mA cm<sup>-2</sup> (with each electroplating/ stripping process lasting 0.5 hours). The LFP/CSE-40%/Li and NCM811/CSE-40%/Li cells were tested within the voltage ranges of 2–4 V vs. Li/Li<sup>+</sup> and 2.8–4.3 V vs. Li/Li<sup>+</sup>, respectively.

To verify the theory that the surface B atoms of amorphous BN nanosheets can adsorb the anion TFSI-with O atoms and demonstrate the reason for the higher lithium ion transference number compared to crystalline BN nanosheets. The DFT-based atomic adsorption energy was used to calculate the adsorption energy of lithium ions on N atoms.

## Supporting Information

Supporting Information is available from the Wiley Online Library or from the author.

## Acknowledgements

This work was supported by Guangdong Provincial Key Laboratory of Materials and Technology for Energy Conversion (Grant No. MATEC2023KF010), Guangdong Basic and Applied Basic Research Foundation (Grant No. 2022A1515010015), and 2023 Huizhou key areas research and development project (Grant No. 2023DQ010002).

## Conflict of Interests

The authors declare no conflict of interest.

## Data Availability Statement

The data that support the findings of this study are available from the corresponding author upon reasonable request.

**Keywords:** amorphous boron nitride nanosheets • composite solid electrolytes • ionic conductivity • solid-state lithium batteries

- [1] a) Y. Lyu, X. Wu, K. Wang, Z. Feng, T. Cheng, Y. Liu, M. Wang, R. Chen, L. Xu, J. Zhou, Y. Lu, B. Guo, *Adv. Energy Mater.* **2021**, *11*, 2000982; b) J. Xu, X. Cai, S. Cai, Y. Shao, C. Hu, S. Lu, S. Ding, *Energy Environ. Mater.* **2023**, *6*, e12450.
- [2] Y. K. Liu, C. Z. Zhao, J. Du, X. Q. Zhang, A. B. Chen, Q. Zhang, *Small* **2023**, *19*, 2205315.
- [3] a) A. Hu, W. Chen, F. Li, M. He, D. Chen, Y. Li, J. Zhu, Y. Yan, J. Long, Y. Hu, T. Lei, B. Li, X. Wang, J. Xiong, *Adv. Mater.* **2023**, *35*, 2304762; b) L. Han, L. Wang, Z. Chen, Y. Kan, Y. Hu, H. Zhang, X. He, *Adv. Funct. Mater.* **2023**, *33*, 2300892; c) X. Tian, Y. Yi, B. Fang, P. Yang, T. Wang, P. Liu, L. Qu, M. Li, S. Zhang, *Chem. Mater.* **2020**, *32*, 9821; d) K. Deng, Q. Zeng, D. Wang, Z. Liu, G. Wang, Z. Qiu, Y. Zhang, M. Xiao, Y. Meng, *Energy Storage Mater.* **2020**, *32*, 425.
- [4] a) J. Han, M. J. Lee, K. Lee, Y. J. Lee, S. H. Kwon, J. H. Min, E. Lee, W. Lee, S. W. Lee, B. J. Kim, *Adv. Mater.* **2022**, *35*, 2205194; b) X. Zhou, B. Zhang, F. Huang, F. Li, Z. Ma, J. Liu, *Nano Energy* **2023**, *108*, 108221; c) X. Li, Y. Tian, L. Shen, Z. Qu, T. Ma, F. Sun, X. Liu, C. Zhang, J. Shen, X. Li, L. Gao, S. Xiao, T. Liu, Y. Liu, Y. Lu, *Adv. Funct. Mater.* **2021**, *31*, 2009718.
- [5] a) R. DeWees, H. Wang, *ChemSusChem* **2019**, *12*, 3713; b) Z. Jian, Y. S. Hu, X. Ji, W. Chen, *Adv. Mater.* **2017**, *29*, 1601925; c) C. Cui, C. Zeng, G. Huang, X. Feng, Y. Zhang, T. Zhai, H. Li, *Adv. Energy Mater.* **2022**, *12*, 2202250.
- [6] S. Yu, D. J. Siegel, *Chem. Mater.* **2017**, *29*, 9639.
- [7] C. Uhlmann, P. Braun, J. Illig, A. Weber, E. Ivers-Tiffée, *J. Power Sources* **2016**, *307*, 578.
- [8] a) Y. Su, X. Rong, A. Gao, Y. Liu, J. Li, M. Mao, X. Qi, G. Chai, Q. Zhang, L. Suo, L. Gu, H. Li, X. Huang, L. Chen, B. Liu, Y.-S. Hu, *Nat. Commun.* **2022**, *13*, 4181; b) S. Li, Q. Liu, W. Zhang, L. Fan, X. Wang, X. Wang, Z. Shen, X. Zang, Y. Zhao, F. Ma, Y. Lu, *Adv. Sci.* **2021**, *8*, 2003240.
- [9] S. Xu, Z. Sun, C. Sun, F. Li, K. Chen, Z. Zhang, G. Hou, H. M. Cheng, F. Li, *Adv. Funct. Mater.* **2020**, *30*, 2007172.
- [10] Y. Wu, Y. Li, Y. Wang, Q. Liu, Q. Chen, M. Chen, *J. Energy Chem.* **2022**, *64*, 62.
- [11] X. Yu, L. Xue, J. B. Goodenough, A. Manthiram, *Adv. Funct. Mater.* **2021**, *31*, 2002144.
- [12] H. Da, S. Pan, J. Li, J. Huang, X. Yuan, H. Dong, J. Liu, H. Zhang, *Energy Storage Mater.* **2023**, *56*, 457.
- [13] Y. Tang, Y. Xiong, L. Wu, X. Xiong, T. Me, X. Wang, *ACS Appl. Energ. Mater.* **2023**, *6*, 4016.
- [14] a) A. M. Nolan, Y. Zhu, X. He, Q. Bai, Y. Mo, *Joule* **2018**, *2*, 2016; b) T. Famprakis, P. Canepa, J. A. Dawson, M. S. Islam, C. Masquelier, *Nat. Mater.* **2019**, *18*, 1278.
- [15] a) Y. Liu, D. Lin, P. Y. Yuen, K. Liu, J. Xie, R. H. Dauskardt, Y. Cui, *Adv. Mater.* **2016**, *29*, *10*; b) J. Lopez, Y. Sun, D. G. Mackanic, M. Lee, A. M. Foudeh, M. S. Song, Y. Cui, Z. Bao, *Adv. Mater.* **2018**, *30*, 1804142.
- [16] a) S. Su, J. Ma, L. Zhao, K. Lin, Q. Li, S. Lv, F. Kang, Y. B. He, *Carbon Energy* **2021**, *3*, 866; b) K. J. Kim, M. Balaish, M. Wadaguchi, L. Kong, J. L. M. Rupp, *Adv. Energy Mater.* **2021**, *11*, 2002689; c) X. Han, Y. Gong, K. Fu, X. He, G. T. Hitz, J. Dai, A. Pearse, B. Liu, H. Wang, G. Rubloff, Y. Mo, V. Thangadurai, E. D. Wachsman, L. Hu, *Nat. Mater.* **2016**, *16*, 572.
- [17] L.-Z. Fan, H. He, C.-W. Nan, *Nat. Rev. Mater.* **2021**, *6*, 1003.
- [18] a) S. Liu, W. Liu, D. Ba, Y. Zhao, Y. Ye, Y. Li, J. Liu, *Adv. Mater.* **2023**, *35*, 2110423; b) J. Shim, H. J. Kim, B. G. Kim, Y. S. Kim, D.-G. Kim, J.-C. Lee, *Energy Environ. Sci.* **2017**, *10*, 1911.
- [19] T. Pareek, S. Dwivedi, S. A. Ahmad, M. Badole, S. Kumar, *J. Alloys Compd.* **2020**, *824*, 153991.
- [20] K. J. Harry, D. T. Hallinan, D. Y. Parkinson, A. A. MacDowell, N. P. Balsara, *Nat. Mater.* **2013**, *13*, 69.
- [21] a) L. Yang, Z. Wang, Y. Feng, R. Tan, Y. Zuo, R. Gao, Y. Zhao, L. Han, Z. Wang, F. Pan, *Adv. Energy Mater.* **2017**, *7*, 1701437; b) F. Croce, G. B. Appetecchi, L. Persi, B. Scrosati, *Nature* **1998**, *394*, 456.
- [22] H. Huo, Y. Chen, J. Luo, X. Yang, X. Guo, X. Sun, *Adv. Energy Mater.* **2019**, *9*, 1804004.
- [23] J. Bae, Y. Li, F. Zhao, X. Zhou, Y. Ding, G. Yu, *Energy Storage Mater.* **2018**, *15*, 46.
- [24] Z. Lin, C. Du, B. Yan, C. Wang, G. Yang, *Nat. Commun.* **2018**, *9*, 4036.
- [25] a) M. G. Rasul, A. Kiziltas, B. Arfaei, R. Shahbazian-Yassar, *NPJ 2D Mater. Appl.* **2021**, *5*, 56; b) G. Wu, X. Zheng, P. Cui, H. Jiang, X. Wang, Y. Qu, W. Chen, Y. Lin, H. Li, X. Han, Y. Hu, P. Liu, Q. Zhang, J. Ge, Y. Yao, R. Sun, Y. Wu, L. Gu, X. Hong, Y. Li, *Nat. Commun.* **2019**, *10*, 4855.
- [26] K. S. Novoselov, A. K. Geim, S. V. Morozov, D. Jiang, Y. Zhang, S. V. Dubonos, I. V. Grigorieva, A. A. Firsov, *Science* **2004**, *306*, 666.
- [27] Y. Hernandez, V. Nicolosi, M. Lotya, F. M. Blighe, Z. Sun, S. De, I. T. McGovern, B. Holland, M. Byrne, Y. K. Gun'Ko, J. J. Boland, P. Niraj, G. Duesberg, S. Krishnamurthy, R. Goodhue, J. Hutchison, V. Scardaci, A. C. Ferrari, J. N. Coleman, *Nat. Nanotechnol.* **2008**, *3*, 563.
- [28] O. B. Chae, J. Kim, I. Park, H. Jeong, J. H. Ku, J. H. Ryu, K. Kang, S. M. Oh, *Chem. Mater.* **2014**, *26*, 5874.
- [29] R. Sun, J. Gao, G. Wu, P. Liu, W. Guo, H. Zhou, J. Ge, Y. Hu, Z. Xue, H. Li, P. Cui, X. Zheng, Y. Wu, G. Zhang, X. Hong, *Cell Rep. Phys. Sci.* **2020**, *1*, 7.
- [30] C. Zhao, H. Zhang, W. Si, H. Wu, *Nat. Commun.* **2016**, *7*, 12543.
- [31] W. Lei, V. N. Mochalin, D. Liu, S. Qin, Y. Gogotsi, Y. Chen, *Nat. Commun.* **2015**, *6*, 8849.
- [32] C. Deng, Y. Gao, Y. Yao, B. Liang, S. Lu, T. Tao, *J. Mater. Chem. A* **2022**, *10*, 11766.
- [33] a) P. Xiong, B. Sun, N. Sakai, R. Ma, T. Sasaki, S. Wang, J. Zhang, G. Wang, *Adv. Mater.* **2020**, *32*, 1902654; b) A. Castellanos-Gomez, M. Poot, G. A. Steele, H. S. J. van der Zant, N. Agrait, G. Rubio-Bollinger, *Adv. Mater.* **2012**, *24*, 772.
- [34] S. Hong, C.-S. Lee, M.-H. Lee, Y. Lee, K. Y. Ma, G. Kim, S. I. Yoon, K. Ihm, K.-J. Kim, T. J. Shin, S. W. Kim, E.-C. Jeon, H. Jeon, J.-Y. Kim, H.-I. Lee, Z. Lee, A. Antidormi, S. Roche, M. Chhowalla, H.-J. Shin, H. S. Shin, *Nature* **2020**, *582*, 511.
- [35] Z. Yang, J. Hao, S. Yuan, S. Lin, H. M. Yau, J. Dai, S. P. Lau, *Adv. Mater.* **2015**, *27*, 3748.
- [36] Q. Weng, X. Wang, X. Wang, Y. Bando, D. Golberg, *Chem. Soc. Rev.* **2016**, *45*, 3989.
- [37] M. Cargnello, J. J. D. Jaén, J. C. H. Garrido, K. Bakhmutsky, T. Montini, J. J. C. Gámez, R. J. Gorte, P. Fornasiero, *Science* **2012**, *337*, 713.
- [38] H. Zhao, Y. Yue, Y. Zhang, L. Li, L. Guo, *Adv. Mater.* **2016**, *28*, 2037.
- [39] X.-y. Hu, M.-x. Jing, H. Yang, Q.-y. Liu, F. Chen, W.-Y. Yuan, L. Kang, D.-H. Li, X.-Q. Shen, *J. Colloid Interface Sci.* **2021**, *590*, 50.
- [40] H. Maleki Kheimeh Sari, X. Li, *Adv. Energy Mater.* **2019**, *9*, 1901597.

Manuscript received: May 5, 2024

Accepted manuscript online: May 16, 2024

Version of record online: July 16, 2024